Proceedings of the ASME 2010 3rd Joint US-European Fluids Engineering Summer Meeting and 8th International Conference on Nanochannels, Microchannels, and Minichannels
FEDSM-ICNMM2010
August 1-5, 2010, Montreal, Canada

FEDSM-ICNMM2010-30791

ANALYSIS OF TURBULENCE IN THE TIP REGION OF A WATERJET PUMP ROTOR

Huixuan Wu
Dept. of Mechanical Engineering
The Johns Hopkins University
Baltimore, MD, USA

Rinaldo L Miorini
Dept. of Mechanical Engineering
The Johns Hopkins University
Baltimore, MD, USA

Joseph Katz
Dept. of Mechanical Engineering
The Johns Hopkins University
Baltimore, MD, USA

ABSTRACT

A series of high resolution planar particle image velocimetry measurements performed in a waterjet pump rotor reveal the inner structure of the tip leakage vortex (TLV) which dominates the entire flow field in the tip region. Turbulence generated by interactions among the TLV, the shear layer that develops as the backward leakage flow emerges from the tip clearance as a "wall jet", the passage flow, and the endwall is highly inhomogeneous and anisotropic. We examine this turbulence in both RANS and LES modelling contexts. Spatially non-uniform distributions of Reynolds stress components are explained in terms of the local mean strain field and associated turbulence production. Characteristic length scales are also inferred from spectral analysis. Spatial filtering of instantaneous data enables the calculation of subgrid scale (SGS) stresses, along with the SGS energy flux (dissipation). The data show that the SGS energy flux differs from the turbulence production rate both in trends and magnitude. The latter is dominated by energy flux from the mean flow to the large scale turbulence, which is resolved in LES, whereas the former is dominated by energy flux from the mean flow to the SGS turbulence. The SGS dissipation rate is also used for calculating the static and dynamic Smagorinsky coefficients, the latter involving filtering at multiple scales; both vary substantially in the tip region, and neither is equal to values obtained in isotropic turbulence.

NOMENCLATURE

z, r, θ	Axial, radial, circumferential coordinate
c	Chord-length of the tip profile
s	Linear coordinate along the tip chord
h	Tip clearance width
γ	Stagger angle of the blade profile
ϕ	Rotor phase
u_z, u_r, u_θ	Axial, radial, circumf. velocity components
U_z, U_r, U_θ	Mean flow velocity components
U_{TIP}	Tip speed
τ_{ij}	SGS stress tensor
Π_{2D}	SGS dissipation rate
ν_T	Eddy viscosity
ω_θ	Circumferential vorticity
S_{ij}	Strain rate tensor
k_{2D}	In-plane TKE
P_{2D}	In-plane TKE production rate
δ	Vector spacing
Δ	Spatial box filter size
$C_s(C_{s,Dyn})$	Ensemble averaged static (dynamic) Smagorinsky coefficient

1 INTRODUCTION

Tip leakage flow through the clearance between the blade tip and the casing endwall is an inherent phenomenon in turbomachines with unshrouded rotor [1, 2]. It is driven by the pressure difference between the blade pressure side (PS) and suction side (SS). This flow rolls up into a tip leakage vortex (TLV), causing several adverse effects, e.g. shifting of the working point due to blockage [3] and efficiency losses caused by the turbulent flows involved [3-5]. However, thorough analyses of this tip flow is quite limited since high spatial resolution time-resolved experimental data are not yet available, while fully resolved direct numerical simulations are not feasible due to complex boundary geometry and high Reynolds number. Interpreting of the limited available data and modeling this flow are major challenges due to the

simultaneous existence of several flow structures and the complex interactions among them.

Recent experimental studies of tip flow have involved direct pressure and velocity measurements in the rotor passage (e.g. [6-8]) or in linear cascades (e.g. [9-11]). Numerical methods include Reynolds Average Navier Stokes (RANS, e.g. [12, 13]) and Large Eddy Simulations (LES, e.g. [14-17]). Detailed experimental data that resolve the leakage flow, rollup process of a TLV and its inner structure are still missing. To address this problem, we have recently performed a series of high resolution planar particle image velocimetry (PIV) measurements in the tip region of a waterjet pump rotor blade. Optical access to the tip region has been facilitated by matching the refractive index of the fluid with that of the acrylic blades and pump casing. An analysis of velocity and vorticity distributions in several meridional planes along the blade passage can be found in [18] and [19]. As discussed in these papers, in our system, the TLV starts rolling up at about one third of the blade chordlength and gains strength by engulfing circulation shed from the blade. Further downstream, the TLV detaches from the blade tip SS corner and migrates towards the PS of the neighboring blade because of the induced motion caused by its "mirror image," which is located inside the pump casing wall. This vortex subsequently bursts into a "cloud" of vortex fragments, presumably because of adverse pressure gradients in the aft part of the rotor passage. These observations are consistent with previous results. For example, TLV migration is described in a review by Tan [2], vorticity engulfment after rollup and secondary flow induced by TLV are analyzed by You [17], and the TLV burst at the aft part of the passage is shown by Yu and Liu [8].

In this paper, we focus on the turbulence generation and distribution in the tip region. We first calculate the Reynolds stresses $< u_i' u_j' >$ and production rates of each component [20]:

$$P_{ij} = - < u_i' u_k' > \partial U_j / \partial x_k - < u_j' u_k' > \partial U_i / \partial x_k \quad (1)$$

where $U_j(x_i, \phi)$ is the phase averaged velocity at a certain location x_i , ϕ is the phase, $u_i' = u_i - U_i$ is the velocity fluctuation, and < > indicates ensemble averaging. Results are then used to evaluate reasons for the turbulence anisotropy in the tip region. We subsequently examine the kinetic energy spectra of this anisotropic turbulence and estimate the Kolmogorov scales in the vicinity of the TLV. To examine the turbulence in the context of LES, which resolves only large-scale motions and models the effects of SGS structures based on the resolved flow dynamics [20, 21], we spatially filter the data using a box filter. Spatial filtering of Navier Stokes equations introduces the SGS stress, $\tau_{ij} = \widetilde{u_i u_j} - \tilde{u}_i \tilde{u}_j$, here $\sim$ indicates spatial filtering. The energy flux from resolved to subgrid scales, the so-called SGS dissipation rate, is defined as:

$$\Pi = - < \tau_{ij} \tilde{S}_{ij} >$$

where $S_{ij} = 0.5(\partial u_i / \partial x_j + \partial u_j / \partial x_i)$ is the strain rate tensor. In order to close the momentum equation in LES, it is necessary to model τ_{ij} based on variables of the resolved velocity field. The most popular SGS stress model is the Smagorinsky (eddy viscosity) Model [22],

$$\tau_{ij}^d = -2\nu_T \tilde{S}_{ij} \qquad \nu_T = (C_S \Delta)^2 |\tilde{S}|$$

where $\tau_{ij}^d = \tau_{ij} - \frac{1}{3}\tau_{kk}\delta_{ij}$ is the deviatoric part of the SGS stress tensor, C_s is the (static) Smagorinsky coefficient, $|\tilde{S}| = (2\tilde{S}_{ij}\tilde{S}_{ij})^{0.5}$, and Δ is the filter size. For homogeneous and isotropic flow, $C_s \approx 0.16$, as determined by matching the real SGS energy flux with the modeled one, i.e.,

$$C_S^2 = \Pi / < 2\Delta^2 |\tilde{S}| \tilde{S}_{ij} \tilde{S}_{ij} > \quad (2)$$

As an alternative, the dynamic model $C_{S,Dyn}$ is determined based on the instantaneous resolved flow field using

$$C_{S,Dyn}^2 = < L_{ij} M_{ij} > / < M_{ij} M_{ij} > \quad (3)$$

Here, $L_{ij} = \overline{\tilde{u}_i \tilde{u}_j} - \bar{\tilde{u}}_i \bar{\tilde{u}}_j$ and $M_{ij} = -2\tilde{\Delta}^2(\alpha^2 |\bar{\tilde{S}}| \bar{\tilde{S}}_{ij} - \overline{|\tilde{S}| \tilde{S}_{ij}})$, the overbar indicates a second spatial filtering at a scale $\alpha\Delta$. In this paper we also use the experimental data to explain the fundamental differences between turbulent kinetic energy (TKE) production rate and SGS energy flux, following procedures introduced in [23]. We compare different elements of the SGS energy flux, e.g. from the mean flow to the resolved turbulence, and from the mean flow to the SGS turbulence, etc. The measured spatial variations in the magnitudes of ensemble averaged static and dynamic Smagorinsky coefficients, both of which differ substantially from the isotropic turbulence model, also point at potential challenges in applications of LES in turbomachines.

2 FACILITY AND EXPERIMENTAL SETUP

The facility and experimental procedures are described in details by [18] and [19]. Briefly, as illustrated in Fig. 1a, the water-jet pump is located in a closed loop facility, which is a recent upgrade of a version described in [24]. A summary of relevant dimensions of the system is provided in Table 1, and sketches are shown in Figures 1c-f. The pump is driven by a 60 HP AC motor, which is connected to the rotor by a 50.8 mm diameter shaft. A settling chamber containing honeycombs is used for improving the flow uniformity upstream of the pump. The geometry of the pump (AxWJ-1) has been designed at NSWC/Carderock [25]. The nominal tip clearance width for a perfectly centered rotor is 0.7 mm; however, direct measurements performed on PIV images indicate that the tip clearance width of the rotor blade investigated in this paper is 1.0 mm on average. This deviation is a result of slight rotor eccentricity. Shapes of the rotor blade profiles along with the stagger angles at several radial cross sections, which are provided in Figure 1e, show that both the stagger angle and the camber line of the rotor blade change significantly from hub to tip. Downstream of the rotor, the flow is accelerated to a 161.5 mm jet, and the rest of the loop has 304.8 mm diameter piping. The pressure drop in the loop is controlled by an adjustable

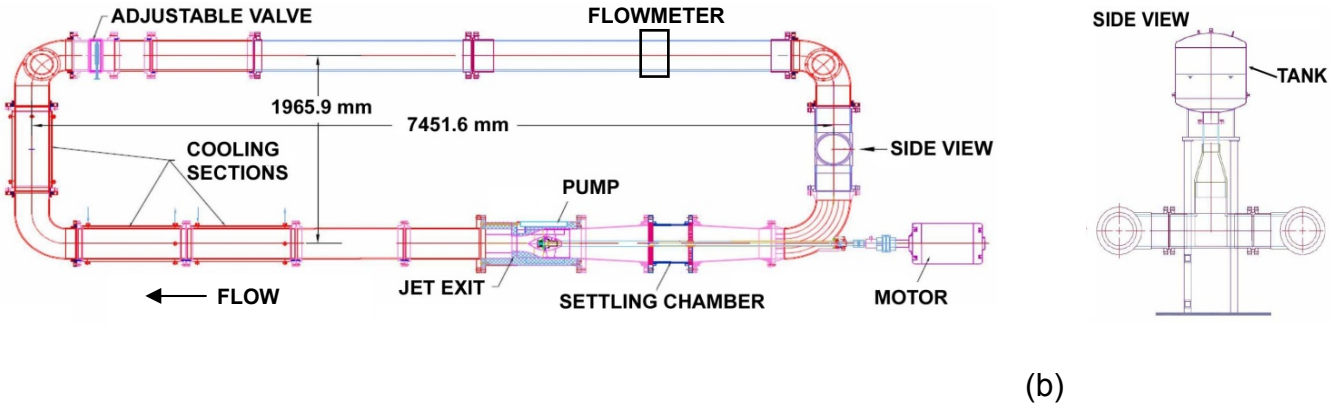

(a) (b)

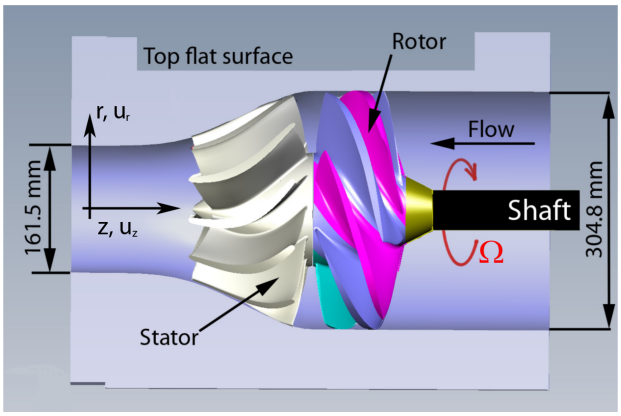

(c)

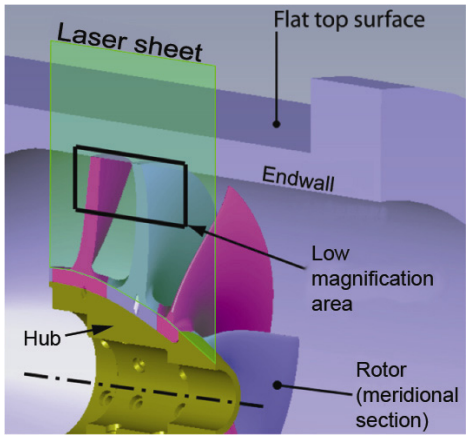

(d)

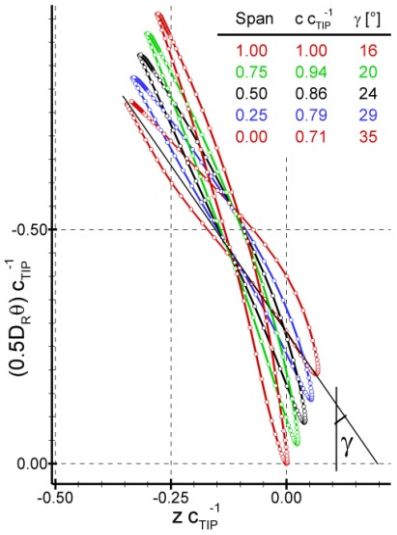

(e)

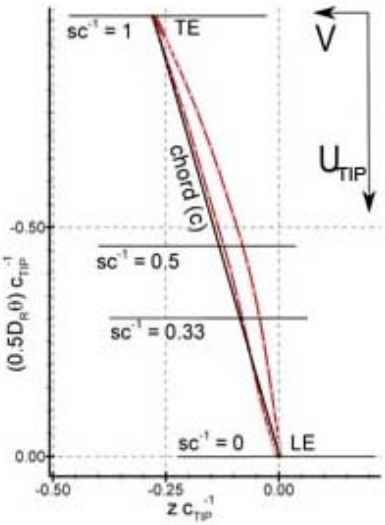

(f)

Fig. 1 Water-jet pump facility and experiment setup: (a) top view of the test loop, (b) side view of the loop, (c) meridional section of the casing hosting the rotor and stator (not sectioned). The global frame of reference is indicated. (d) meridional section of the rotor and PIV laser sheet orientation, (e) rotor blade profiles at different spanwise locations. Note the origin at the tip profile LE, chord middle points are matched by shifting the span < 1 profiles, chordlength and stagger angle γ are indicated. (f) the tip profile is repeated to highlight the chosen convention for the chord fraction sc^{-1}. Horizontal lines indicate the trace of the laser sheet intersecting the tip profile at different chord fractions.

Tab.1 Rotor geometry and reference data

Number of rotor blades	7
Number of stator blades	11
Tip profile chord length c	267.2 mm
Tip profile axial chord length c_A	74.5 mm
Stagger angle $\sin\gamma=(c_A/c)$	16.2°
Rotor diameter D_R	303.4 mm
Casing diameter ($2R$)	304.8 mm
Jet exit diameter	161.5 mm
Blade span at leading edge	123.2 mm
Blade span at trailing edge	79.3 mm
Tip clearance (nominal)	0.7 mm
Tip clearance (actual)[1] h	1.0 mm
Clearance ratio (actual) $2hD^{-1}$	6.6×10^{-3}
Blade pitch at the tip ς	136.1 mm
Solidity at the tip $c\varsigma^{-1}$	1.96
Rotor angular velocity Ω	94.2 rads^{-1}(900 rpm)
Tip velocity U_{TIP}	14.36 ms^{-1}
Flow rate Q $[V/U_{TIP}]$	0.157 m^{3}s^{-1} [0.15]
Head rise H	3.7 m
Flow coefficient $\varphi=(2\pi)Q\Omega^{-1}D^{-3}$	0.37
Head coefficient $\psi=(2\pi)^2 gH(\Omega D)^{-2}$	1.7
Torque coefficient $k_T=(2\pi)^2 T\rho^{-1}\Omega^{-2}D^{-5}$	0.14
Efficiency $\eta=\rho gHQ(T\Omega)^{-1}$	0.69
Blade chord Reynolds no. $\mathrm{Re}_C=U_{TIP}c\nu^{-1}$	3.5×10^6
Inflow Re no. $\mathrm{Re}_{IN}=4QD\,[\pi(D^2-d_{SHAFT}^2)\nu]^{-1}$	6.1×10^5

[1]At the measurement point, due to rotor eccentricity

valve. The flow rate is measured by a transit time flowmeter (*Dynasonics TFLX*), and pressures are recorded by a transducer connected to several taps located around the test section. The top of a half-filled tank (Fig. 1b) is connected to a vacuum pump and a pressurized Nitrogen line for controlling the mean pressure in the facility. The pump blades and casing are made of transparent acrylic whose optical refractive index is matched with that of the fluid – a concentrated solution of sodium iodide in water (62% - 64% by weight). The specific gravity of this solution is 1.8 and its kinematic viscosity is 1.1×10^{-6} m^{2}s^{-1} [24], i.e. very close to that of water. Matching of refractive indices enables us to perform unobstructed optical measurements essentially everywhere in the pump through wide flat windows on two sides of the casing. The present measurements are performed at a shaft speed of 900 rpm, slightly above design conditions. The relevant parameters, including tip speed, flow and head coefficients are provided in Table 1.

The investigated area lies on the vertical meridional plane near the endwall (Fig. 1d). To perform PIV measurements, this area is illuminated by a 1 mm thick laser sheet, and the flow is seeded with 13 μm, silver-coated hollow glass spherical particles that have a specific gravity of 1.6. The particle concentration is enough to guarantee that at least 5 particles exist in each PIV interrogation window after image enhancement. Synchronizing the rotor phase with the PIV system enables us to perform PIV measurements at any desired rotor phase, which is defined using the chord fraction sc^{-1}, where s is a coordinate aligned with the blade chord and c is the chordlength (Fig. 1f). Note that measurements are carried out at the meridional plane, which is not perpendicular to the blade chord. Here sc^{-1} simply means that the laser sheet dissects the blade at certain point on the chord. Twenty-five investigated planes at different sc^{-1} are evenly spaced by $0.06c$: 18 along the chord, 3 in front of the leading edge, and 4 beyond the trailing edge. At least 1000 velocity distributions are obtained in each plane. Data are presented in cylindrical coordinates (r, θ, z), as defined in Fig. 1c, and the meridional plane velocity components are denoted as U_z and U_r. The $z = 0$ point is matched with the leading edge of the rotor tip (Fig. 1f).

Image pairs are processed in order to maximize the cross correlation algorithm performance. Since the endwall and blade section contours are visible in images as dim lines (due to slight refractive index mismatch), they are masked out. In order to eliminate the resulting non-uniform background luminance, a 13×13 pixel median-filtered image is subtracted from the original [24]. Subsequently, the images are processed with the Modified Histogram Equalization (MHE) algorithm [26], which locally equalizes the brightness of particle traces. Finally, a Gaussian filter with 0.55 standard deviation is used to smooth the transition between the edge of particle traces and black background. A multi-pass FFT-based cross correlation algorithm (*LaVision© Davis*) is used for calculating the velocity, we set a final interrogation window size of 32×32 pixel and 50% overlap. We have recorded data at three different magnifications. The lowest one, which covers one rotor passage, has a 44×44 mm field of view and vector spacing of 340 μm. The medium resolution data focuses on the TLV center area with a total field of view of 15×15 mm, and vector spacing of 120 μm. In order to resolve the flow details near the tip gap, the highest magnification is obtained using a larger CCD sensor; the field of view is 24×16 mm and the vector spacing is 78 μm. The typical uncertainty in instantaneous displacement measurements is about 0.1~0.15 pixels [24, 26], corresponding to 1.25~2% of the measured value. After ensemble averaging of 1000 realizations, the mean flow quantities are an order of magnitude more accurate.

3 MEAN FLOW STRUCTURES AND TURBULENCE STATISTICS

3.1 Vorticity, Reynolds stress and turbulent kinetic energy distribution

We use the tip velocity (U_{TIP} =14.36 ms^{-1}) and gap size (h=1 mm) to normalize the phase averaged mean flow and

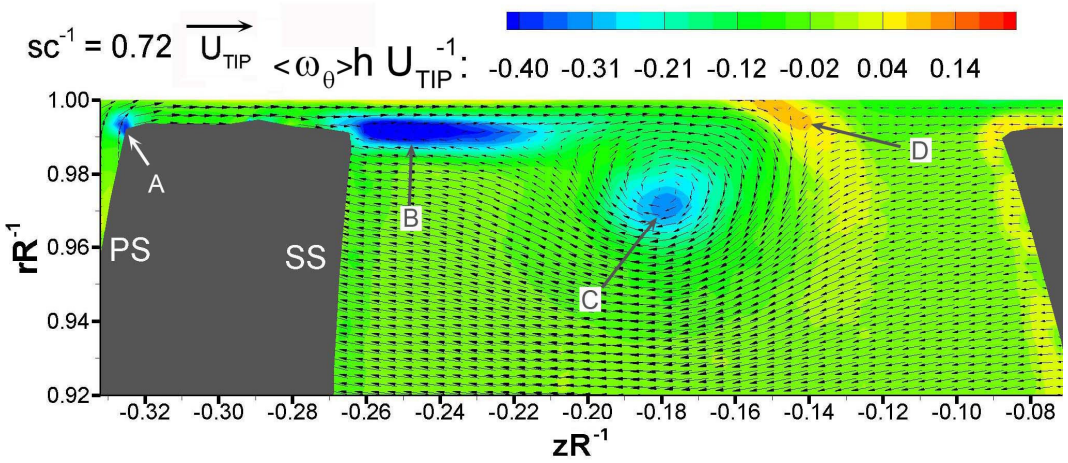

Fig. 2 Phase averaged meridional velocity and circumferential vorticity at sc^{-1}=0.72 obtained at the lowest resolution [18]. Velocity vectors are diluted horizontally 1:2 for clarity. A: Negative vorticity peak at the PS corner. B: Highly vortical (negative) shear layer. C: TLV center. D: Detachment and entrainment of endwall vorticity.

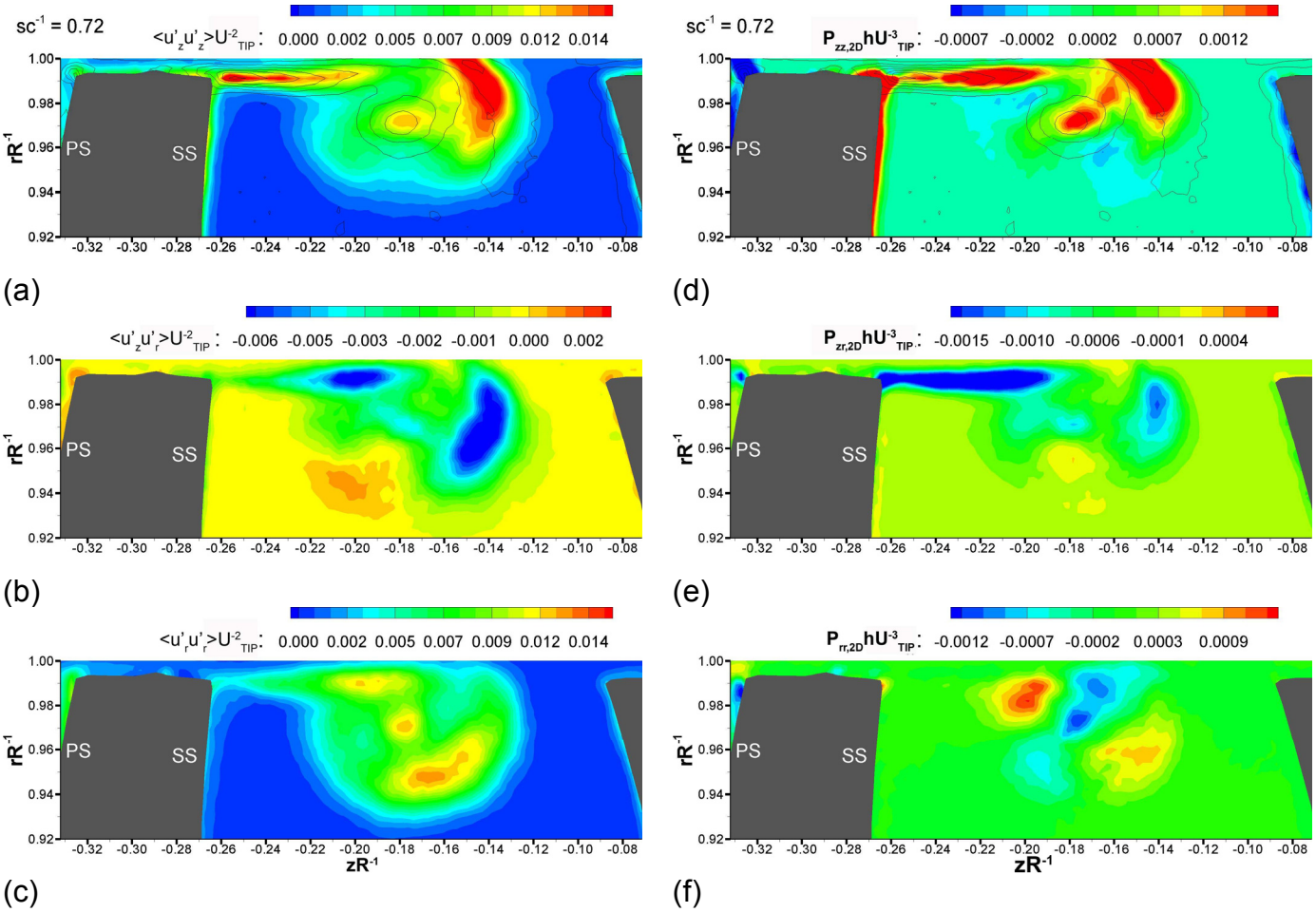

Fig. 3 Left: (a) $\langle u'_z u'_z \rangle$, (b) $\langle u'_z u'_r \rangle$, and (c) $\langle u'_r u'_r \rangle$. Right: Corresponding Reynolds stress production rates: (d) $P_{zz,2D}$, (e) $P_{zr,2D}$, and (f) $P_{rr,2D}$. Results are presented with different scale to highlight spatial transitions. Black iso-vorticity lines in (a) and (d) help locate the TLV.

turbulence variables, i.e.. data are presented as U/U_{TIP}, $-<u_i'u_j'>/U_{TIP}^2$, $\omega_\theta h/U_{TIP} = h(\partial U_r/\partial z - \partial U_z/\partial r)/U_{TIP}$, etc. Since we only have 2D data available, we replace several variables with 2D surrogates, e.g. the TKE is replaced with $k_{2D}/U_{TIP}^2 = (<u_z'u_z'> + <u_r'u_r'>)/2U_{TIP}^2$. A series of phase averaged velocity and vorticity distributions can be found in [18]. In this paper, we select one of these planes for a rigorous analysis. A sample, low-resolution, mean velocity and vorticity distribution at sc^{-1}=0.72 (prior to the TLV burst) is shown in Fig. 2. The backflow from the PS to SS within the blade tip gap is clearly evident, along with a negative vorticity peak in the PS tip corner (point A), in the shear layer (B) developing at the interface between the leakage flow and the passage flow, and the TLV core (C). Another shear layer with positive vorticity (D) is generated to the right of the TLV center, as the casing backflow boundary layer separates and is entrained into the TLV outer perimeter. In the rest of this paper, we refer to these two shear layers as "negative shear layer" and "positive shear layer" respectively.

Reynolds stress distributions along with their corresponding production rates are displayed in Fig. 3. Each of the production rate terms (Eqn. 1) is replaced with its 2D surrogate, i.e.

$$P_{zz,2D} = -2(<u_z'u_z'>\partial U_z/\partial z + <u_z'u_r'>\partial U_z/\partial r)$$
$$P_{zr,2D} = -(<u_z'u_z'>\partial U_r/\partial z + <u_z'u_r'>\partial U_r/\partial r) - (<u_r'u_z'>\partial U_z/\partial z + <u_r'u_r'>\partial U_z/\partial r)$$
$$P_{rr,2D} = -2(<u_r'u_z'>\partial U_r/\partial z + <u_r'u_r'>\partial U_r/\partial r)$$

The values of normalized $<u_z'u_z'>$ peak in the negative shear layer extending from the SS corner since strong radial gradients of axial velocity and shear stress generate high shear production there, i.e. the $-\langle u_z'u_r'\rangle\partial U_z/\partial r$ term in $P_{zz,2D}$. Values of $<u_z'u_z'>$ are also high to the left of the positive shear layer, but here the contraction term $-\langle u_z'u_z'\rangle\partial U_z/\partial z$ dominates near the casing endwall in the region where the backward leakage and passage flows impinge. Away from the wall, shear production at the interface between positive shear layer and negative vorticity near the vortex center is the main contributor. As expected, $<u_z'u_r'>$ is high in the negative shear layers, mainly due to $-<u_r'u_r'>\partial U_z/\partial r$ contribution. In the entrained casing boundary layer, $-<u_z'u_z'>\partial U_r/\partial z$ is the primary contributor. Note that the negative values of $P_{zr,2D}$ are consistent with the definition of the corresponding stress $<u_z'u_r'>$ and the present coordinate system, e.g. both $\partial U_z/\partial r$ and $<u_r'u_r'>$ are positive in the shear layer; consequently, the production term is negative. The distribution of $<u_r'u_r'>$ has three maxima, but their magnitudes are much smaller than those of $<u_z'u_z'>$. Comparing $<u_r'u_r'>$ with its production rate, it is evident that their distributions are not consistent, unlike the other

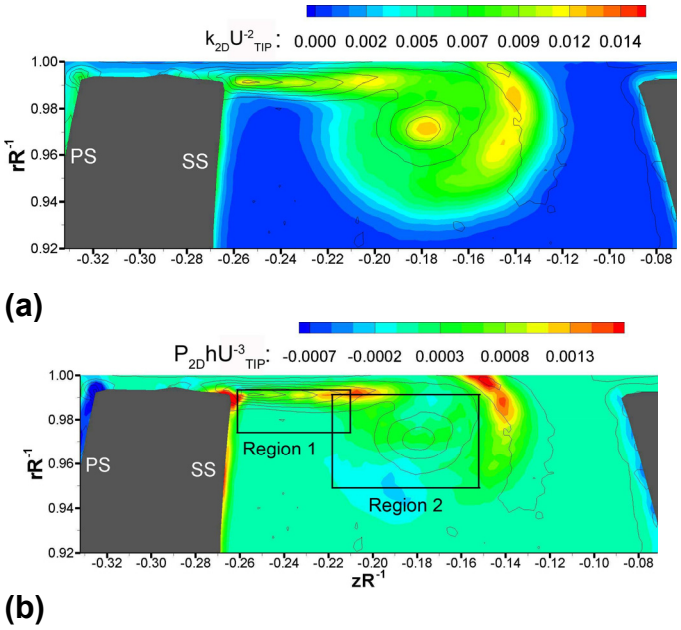

Fig. 4 (a) Planar TKE and (b) planar TKE production rate. Black thin iso-vorticity lines indicate the position of tip and endwall vorticity sheets as well as the TLV core. Black boxes highlight regions where high and medium resolution data have been recorded.

components. Particularly near the TLV center $P_{rr,2D}$ is negative, but $<u_r'u_r'>$ is inherently positive. A likely explanation for this discrepancy is the so-called inter-component energy transfer, i.e. that some of the high $<u_z'u_z'>$ near the center is converted into $<u_r'u_r'>$ by the pressure-rate of strain terms in the evolution equations of Reynolds stresses. In this case, the high positive $P_{zz,2D}$ is a source, and negative $P_{rr,2D}$ is a sink. Note that $<u_z'u_z'>$ and $<u_r'u_r'>$ are of the same order of magnitude near the TLV center, i.e. they have similar contributions to the total TKE (Fig. 4a), but the total TKE production rate there, $P_{2D} = 0.5(P_{zz,2D} + P_{rr,2D})$, is very small since $P_{zz,2D}$ and $P_{rr,2D}$ cancel each other as shown Fig. 4b. In Miorini *et al.* [18], we have already realized that the TKE peak at the TLV center is a result of advection of turbulence generated in the negative shear layer. Anywhere else in the vicinity of the TLV, trends of $<u_r'u_r'>$ and $<u_z'u_z'>$ along with their production terms are very different, clearly indicating that realistic Reynolds stress modeling should treat each of these components separately.

3.2 Spectra and dissipation rate

As expected, the strong non-homogeneity in turbulence results in significant differences among energy TKE spectra measured in different regions of the flow field. We calculate the longitudinal energy spectra using the data measured along the two sample lines shown in Fig. 5c labeled A1-A2 and B1-B2.

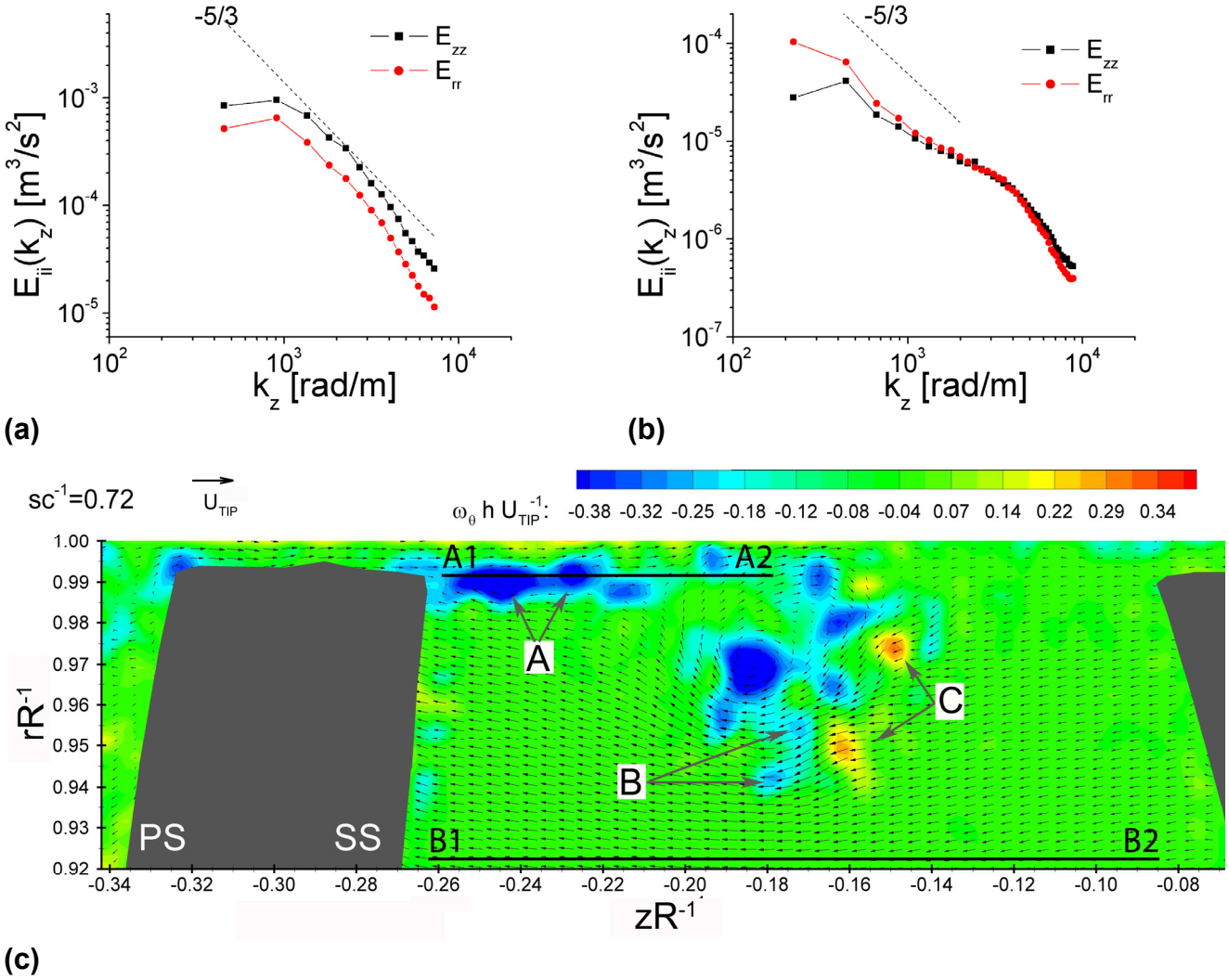

Fig. 5. Turbulence energy spectra calculated over the (a) A1-A2 and (b) B1-B2 lines indicated in (c). (c) a sample instantaneous velocity and circumferential vorticity [19]. A: vortex filament sections in the shear layer, B: filament sections in the TLV center, and C: counter-rotating vortices entrained into the TLV outer perimeter. Vectors are diluted horizontally by 1:2 for clarity.

The first is aligned with the negative shear layer, along the most homogeneous direction that we can define for this flow. The second line is located outside of the TLV, and represents a relatively low turbulence domain. To calculate spectra, we use FFT functions available in Matlab after subtracting the mean velocity and detrending the data. Results are presented in Fig. 5a and b. In the shear layer, the slope in part of the spectra of the two velocity components is close to -5/3. However, $E_{rr}(k_z)$ is smaller than $E_{zz}(k_z)$, in contrast to trends of isotropic turbulence ($E_{rr}(k_z) \approx 4/3\ E_{zz}(k_z)$ [20]), clearly indicating that the turbulence is far from being isotropic, consistently with the high shear stress there. Nevertheless, we use isotropic turbulence theory to estimate the order of magnitude of dissipation rate, ε, by fitting the -5/3 slope part of the spectrum with

$$E_{11}(k_1) = \frac{18}{55} C_K \varepsilon^{\frac{2}{3}} k^{-\frac{5}{3}} \approx 0.49 \varepsilon^{\frac{2}{3}} k^{-\frac{5}{3}}$$

In the shear layer, we calculate $\varepsilon \approx 2285$ m^{2}s^{-3}, hence, the Kolmogorov length scale $\eta = (\nu^3/\varepsilon)^{0.25}$ is of the order of 5 µm. Clearly, the spatial resolution of our measurements is way too coarse to resolve dissipation-range length scales. The spectra (Fig. 5b) calculated along the B1-B2 line has a slope close to $-5/3$ for $k_1 < 10^3$, i.e. at the large scale turbulence, with estimated $\eta = 35$ µm. Note that $E_{rr}(k_z) > E_{zz}(k_z)$ indicates a state of weak turbulence anisotropy. Thus, for this region, the

present high-resolution data (not the one used for generating Figures 3-6), already resolves a substantial fraction of the turbulence dissipation range. However, at higher wavenumbers, there is a spectral bump centered around 4×10^3 rad/m. As shown in Wu *et al*. [19] and illustrated by an example also in Fig. 5c, the instantaneous vorticity distribution shows that both the TLV and the shear layer contain vortex filaments whose characteristic diameter is about 2 mm, i.e. at the length scale corresponding to the spectral bump. This coincidence indicates that the velocity fluctuation near the B1-B2 line is strongly affected by induced motion due to interlaced vortex filaments located within the TLV.

4 SUBGRID STRESSES AND ASSOCIATED MODELING ISSUES

4.1 SGS dissipation

To calculate the SGS stresses, we apply a spatial box filter with size Δ on the velocity field in regions that are located sufficiently away from the solid boundaries. The filter kernel centered at x_i is $G(x_i-\xi_i)=1/\Delta^2$ for $|x_i-\xi_i| \le \Delta/2$, i =1 or 2, and $G(x_i-\xi_i)=0$ elsewhere. Since the distribution of Kolmogorov scales is highly inhomogeneous, there is no point in expressing the filter scale in terms of turbulence parameters. Choosing $\Delta=9\delta$, where δ is the vector spacing, and using the high magnification data to calculate the SGS stress components, we apply the filter whose scale is in the order of 20-140η. Similarly to other variables, we compute a 2D surrogate for the SGS dissipation rate

$$\Pi_{2D} = -(<\tau_{11}\tilde{S}_{11}> + <\tau_{22}\tilde{S}_{22}> + 2<\tau_{12}\tilde{S}_{12}>)$$

and the velocity derivative in S_{ij} is computed using center difference on the fine PIV grid. While presenting distributions of this quantity, it is normalized by U_{TIP}^3/h. Fig. 6a and b as well as 7a and b compare distributions of normalized Π_{2D} to those of P_{2D} in the two regions for which we have high magnification data, as defined in Fig. 4b. The first (Fig. 6) covers the negative shear layer, and the second (Fig. 7) focuses on the TLV center. As is evident, both Π_{2D} to those of P_{2D} are high along the center of the shear layer, but Π_{2D} is significantly smaller than the corresponding production rate. Near the TLV center, both the magnitudes and distribution patterns are very different. In both cases, regions with negative values are caused, at least in part, by the missing out of plane components. In an attempt to explain discrepancies between turbulence production rate and SGS energy flux, Chow *et al.* [23] show that these terms represent very different quantities. As an illustration, note that spatial filtering of the velocity field filters out part of the (non-uniform) mean flow along with the small scale turbulence, while conversely ensemble averaging of the flow filters out both the large and small scale turbulence. Furthermore, ensemble averaging of spatially filtered data involves application of two filters, and one should be cautious when such operations are performed on nonlinear terms, such as the kinetic energy. To resolve this challenge, as illustrated in Fig. 8, Chow *et al* [23] show that dual decomposition splits the spatially and ensemble filtered kinetic energy into four parts: Mean Resolved (denoted as ***mr***), Mean Subgrid (***ms***), Fluctuation Resolved (***fr***) and Fluctuation Subgrid (***fs***) whose definitions are

$$\widetilde{<K>} = K_{mr} + K_{ms} + K_{fr} + K_{fs}$$
$$K_{mr} = 0.5<\tilde{u}_i><\tilde{u}_i>$$
$$K_{ms} = 0.5(\widetilde{<u_i><u_i>} - <\tilde{u}_i><\tilde{u}_i>)$$
$$K_{fr} = 0.5<\tilde{u}_i'\tilde{u}_i'>$$
$$K_{fs} = 0.5(\widetilde{<u_i'u_i'>} - <\tilde{u}_i'\tilde{u}'>)$$

The evolution equations for each of these terms introduce five different energy fluxes among them. Denoting them as Π(*source, target*), e.g. Π(***mr, ms***) represents energy flux from K_{mr} to K_{ms}, the definitions of these fluxes are:

$$\Pi(mr,ms) = -\tau_{ij}^M <\tilde{S}_{ij}>$$
$$\Pi(mr,fs) = -\tau_{ij}^f <\tilde{S}_{ij}>$$
$$\Pi(mr,fr) = -<\tilde{u}_i'\tilde{u}_j'><\tilde{S}_{ij}>$$
$$\Pi(ms,fs) = -\widetilde{<u_i'u_j'><S_{ij}>} - (-\widetilde{<u_i'u_j'>}<\tilde{S}_{ij}>)$$
$$\Pi(fr,fs) = -<\tau_{ij}'\tilde{S}_{ij}'>$$

Here $\tau_{ij}^M(x,t) = \widetilde{U_iU_j} - \widetilde{U}_i\widetilde{U}_j$, $\tau_{ij}^f = \widetilde{<u_i'u_j'>} - <\tilde{u}_i'\tilde{u}_j'>$ are the mean and fluctuating SGS stresses respectively, given that $\tau_{ij}' = \tau_{ij} - <\tau_{ij}>$ and $\tilde{S}_{ij}' = \tilde{S}_{ij} - <\tilde{S}_{ij}>$. To reduce the confusion, each of these fluxes is also illustrated in Fig. 8. The SGS dissipation represents all the energy flux from resolved to subgrid scales, i.e.

$$\Pi = \Pi(mr, ms) + \Pi(mr, fs) + \Pi(fr, fs)$$

whereas the TKE production represents all the energy fluxes from the mean to fluctuating energy components, i.e.

$$P = \Pi(mr, fr) + \Pi(ms, fs) + \Pi(ms, fs)$$

As is evident, only one of the three contributors, Π (*mr, fs*), appears in both expressions. Clearly, the SGS dissipation rate represents very different energy fluxes from the TKE production. Fig. 6c-g and 7c-g show the distributions of all the 2D surrogate energy flux terms. In the shear layer, the production rate is dominated by Π_{2D} (*mr, fr*), which is available in LES, but Π_{2D} (*mr, fs*) is also significant. Conversely, Π_{2D} (*mr, fs*) is the main contributor to Π_{2D}, but Π_{2D} (*fr, fs*) and Π_{2D} (*mr, ms*) are not negligible. Note that the latter represents energy flux among different scales of the mean flow, and has nothing to do with the turbulence. In the TLV center, Π_{2D} (*mr, fr*) dominates P_{2D}, while Π_{2D} (*fr, fs*) and Π_{2D} (*mr, fs*) are the main contributors to the SGS dissipation. Note that S_{ij} used in the definition of the fluxes is calculated on PIV fine grid. However, in the LES, only velocity field on a coarse grid can be obtained, and its grid spacing is the same as the filter size here. If we compute S_{ij} on the coarse grid frame, the magnitude of these fluxes vary but the distribution patterns remain similar. More discussions about the effects of coarse and fine grids can be found in [23].

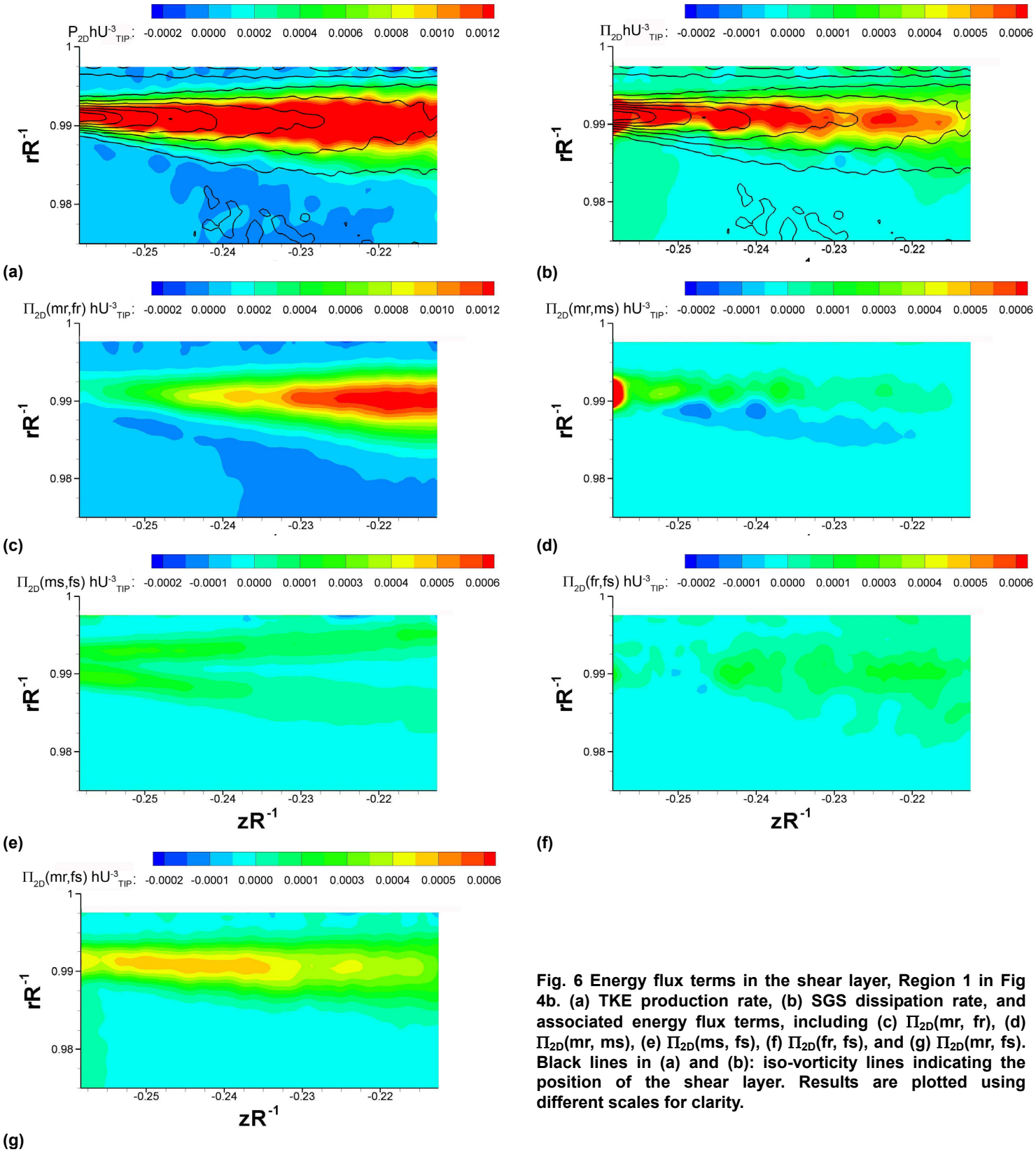

Fig. 6 Energy flux terms in the shear layer, Region 1 in Fig 4b. (a) TKE production rate, (b) SGS dissipation rate, and associated energy flux terms, including (c) Π_{2D}(mr, fr), (d) Π_{2D}(mr, ms), (e) Π_{2D}(ms, fs), (f) Π_{2D}(fr, fs), and (g) Π_{2D}(mr, fs). Black lines in (a) and (b): iso-vorticity lines indicating the position of the shear layer. Results are plotted using different scales for clarity.

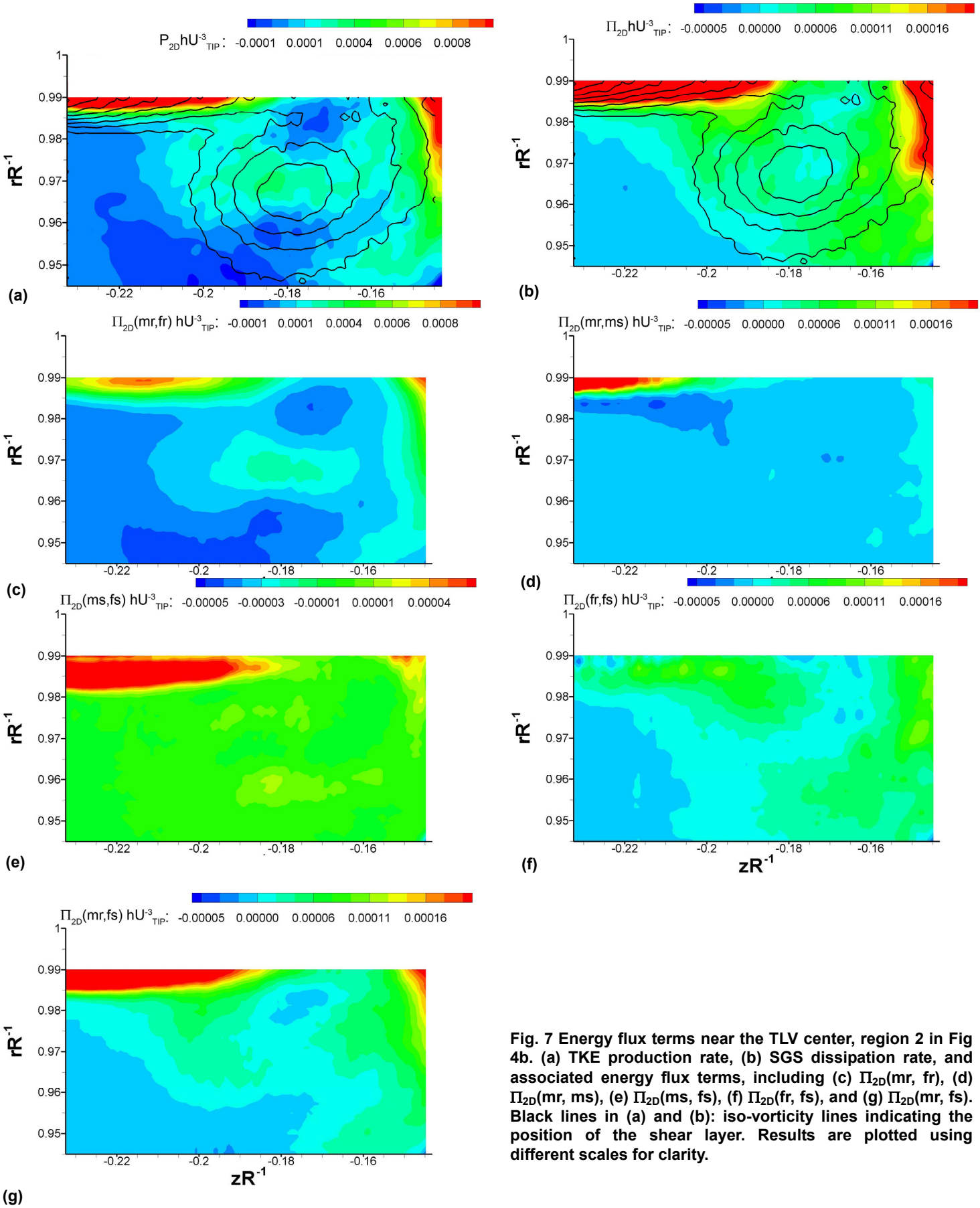

Fig. 7 Energy flux terms near the TLV center, region 2 in Fig 4b. (a) TKE production rate, (b) SGS dissipation rate, and associated energy flux terms, including (c) Π_{2D}(mr, fr), (d) Π_{2D}(mr, ms), (e) Π_{2D}(ms, fs), (f) Π_{2D}(fr, fs), and (g) Π_{2D}(mr, fs). Black lines in (a) and (b): iso-vorticity lines indicating the position of the shear layer. Results are plotted using different scales for clarity.

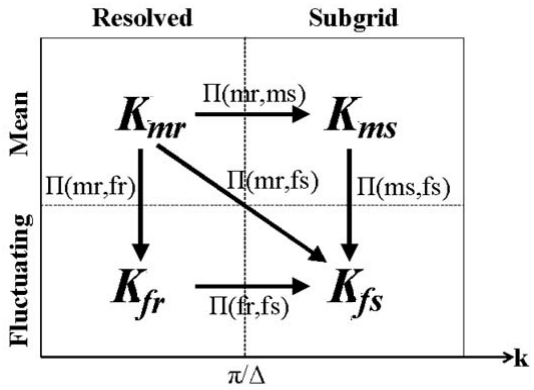

Fig. 8 Schematics of the kinetic energy flux among components of the double filtered flow [23].

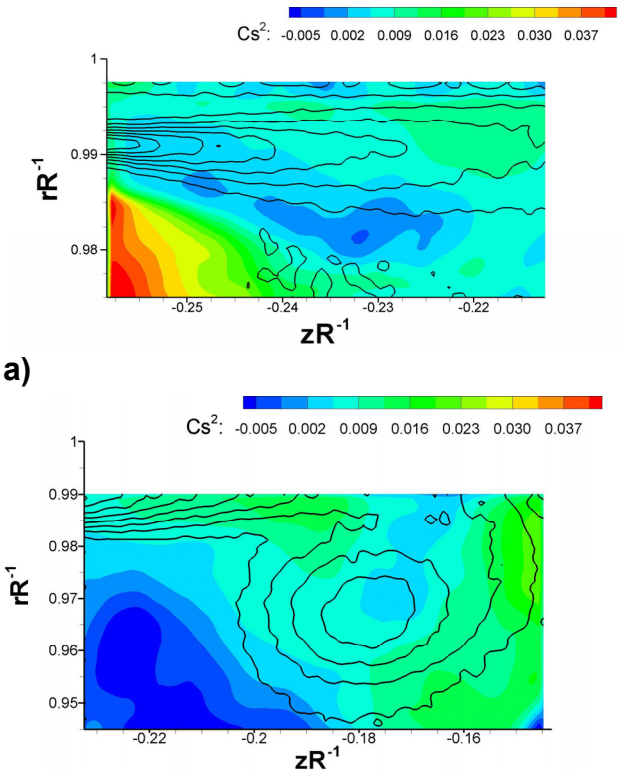

Fig. 9 Distribution of the planar static Smagorinsky coefficient (a) in the shear layer in Region 1 and (b) around the TLV in Region 2. Black Iso-vorticity lines indicate respectively the shear layer and the TLV.

4.2 Measured Model Coefficients

Both the static and dynamic Smagorinsky coefficients vary substantially over the inhomogeneous turbulent field of the tip region. Following Eqn. 2, but using 2D surrogates for the energy terms, we can measure the distributions of these

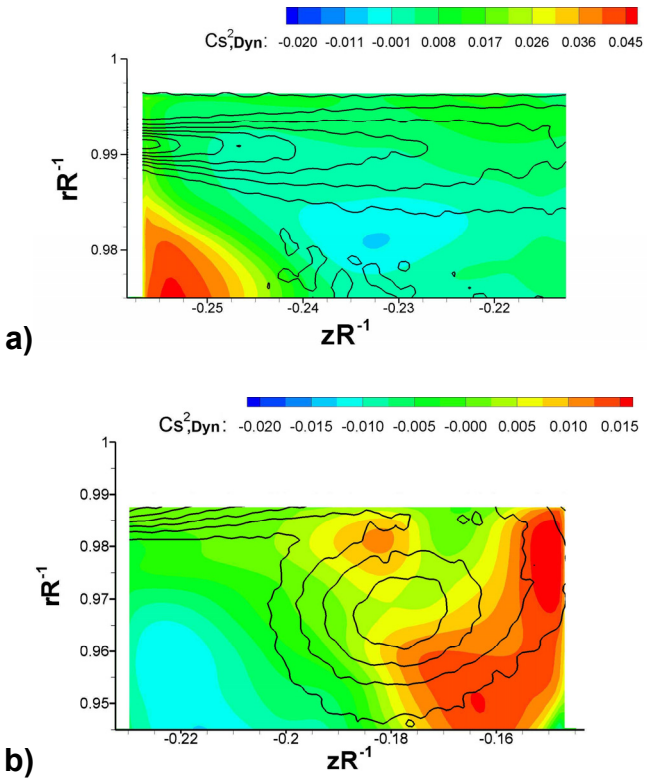

Fig. 10 Distribution of the planar Smagorinsky coefficient calculated using the dynamic model (a) in the shear layer in Region 1 and (b) around the TLV in Region 2. Black Iso-vorticity lines indicate respectively the shear layer and the TLV.

coefficients over high resolution areas. Fig. 9 shows that C_s^2 varies substantially, and is sometimes even negative in the vicinity of the shear layer and TLV. Note that the typical value calculated on isotropic turbulence data is C_s^2=0.026. To calculate the dynamic model coefficients, we filter the data twice at $\Delta=9\delta$ and $\alpha\Delta=17\delta$, following Eqn. 3. The ensemble averaged dynamic model coefficients, shown in Fig 10, have similar spatial trends and magnitudes as the static ones. Clearly, turbulence anisotropy and non-equilibrium conditions near the tip region cause substantial differences between expected to measured values.

5 CONCLUSIONS

This paper is aimed at rigorously analyzing the turbulence in a selected meridional section of a tip leakage vortex that evolves within a water-jet rotor. Most of the data discussed here have been extracted from a set of (relatively) low magnification, planar PIV measurements that cover the entire rotor passage. Additional medium and high magnification data focus on subzones of the same plane, namely the TLV itself and the shear layer feeding vorticity into it, to resolve finer details of the flow. In addition to the vortex, the chosen plane hosts

several other distinct flow structures, such as a shear layer that connects the suction side blade tip to the TLV, and a layer of counter-rotating vorticity detaching from the endwall and entrained into the outer perimeter of the vortex.

Availability of turbulence statistics and spatial gradients of mean flow allows a comparison between spatial trends of Reynolds stress components and turbulent kinetic energy with the corresponding production rates, approximated using 2D surrogates. Trends of $< u_z' u_z' >$, the largest component, and its production rate distributions are consistent in the shear layer and detaching endwall boundary layer. Trends of the shear stress and its production rate are also in agreement in the shear layer. Conversely, the distribution of $< u_r' u_r' >$ is inconsistent with its production rate, indicating that axial-to-radial inter-component energy transfer plays a significant role. In the vicinity of the TLV center, production of $< u_z' u_z' >$ is positive and that of $< u_r' u_r' >$ is negative with a similar magnitude, i.e. they cancel each other in terms of contribution to TKE. Since the shear production there is nearly zero, there is little net turbulence production near the vortex core. Longitudinal turbulent energy spectra evaluated in the shear layer and in the passage flow reveal substantial anisotropy and inhomogeneity in the shear layer along with extremely high dissipation rate. The presence of vortex filaments that occupy the shear layer and TLV center, whose size is of the order of two millimeters, also affects the energy spectra outside of the TLV, presumably due to induced motions.

In the context of LES, using spatial box filters, we also evaluate the distribution of SGS stresses and a 2D surrogate for the SGS dissipation rate. Its distribution is radically different, even in sign, from that of the TKE production rate. To explain this discrepancy, we decompose the spatially and ensemble averaged kinetic energy into four parts and calculate all the energy fluxes among them. This decomposition enables us to realize that the TKE production is dominated by energy flux from mean resolved flow to the resolved turbulence, whereas the SGS dissipation rate is affected by energy flux from the mean resolved flow to the subgrid turbulence, as well as from the resolved to subgrid turbulence. Note that spatial filtering also introduces an SGS mean flow and two associated energy fluxes that are weak in the present system. We also calculate the distributions of ensemble averaged static and dynamic Smagorinsky coefficients (eddy viscosity model). Spatial trends of these quantities are similar, but their magnitudes are different, and both are far from values obtained for isotropic turbulence and typically used in simulations.

ACKNOWLEDGMENTS

This project is sponsored by the Office of Naval Research under grant number N00014-09-1-0353. The program officer is Ki-Han Kim. Funding for the upgrading of test facility is provided by ONR DURIP grant No. N00014-06-1-0556. We would like to thank Yury Ronzhes and Stephen King for their contributions to the construction and maintenance of the facility, as well as to Dr. Francesco Soranna for his assistance in the facility construction, and Kunlun Bai, James Mandaglio and other colleagues for their help in the preparation of the experiments and this paper.

REFERENCE

[1] Lakshminarayana B (1996) Fluid Dynamics and Heat Transfer of Turbomachinery. Wiley Interscience, New York

[2] Tan CS (2006) Three-dimensional and tip clearance flows in compressors, Advances in axial compressor aerodynamics. Von Karman Institute for Fluid Dynamics Lecture Series 2006-06

[3] Denton JD (1993) Loss Mechanisms in Turbomachines. J. Turbomach. 115:621-656

[4] Li YS, Cumpsty NA (1991a) Mixing in Axial Flow Compressors: Part I-Test Facilities and Measurements in a Four-Stage Compressor. J Turbomach 113:161-165

[5] Li YS, Cumpsty NA (1991b) Mixing in Axial Flow Compressors: Part II-Measurements in a Single-Stage Compressor and a Duct. J Turbomach 113:166-174

[6] Xiao X, McCarter AA, Lakshminarayana B (2001) Tip Clearance Effects in a Turbine Rotor: Part I-Pressure field and Loss. J Turbomach. 123: 296-304

[7] Liu B, Wang H, Liu H, Yu H, Jiang H, Chen M (2004) Experimental Investigation of Unsteady Flow Field in the Tip Region of an Axial Compressor Rotor Passage at Near Stall Condition with Stereoscopic Particle Image Velocimetry. J Turbomach. 126:360-374

[8] Yu X, Liu B (2007) Stereoscopic PIV Measurement of Unsteady Flows in an Axial Compressor Stage. Experimental Thermal and Fluid Science 31:1049-1060

[9] Muthanna C, Devenport WJ (2004) Wake of a Compressor Cascade with Tip Gap, Part 1: Mean Flow and Turbulence Structure. AIAA Journal 42:2320-2331

[10] Ma R, Devenport WJ (2007) Tip Gap Effects on the Unsteady Behavior of a Tip Leakage Vortex. AIAA Journal 45:1713-1724

[11] Palafox P, Oldfield MLG, LaGraff JE, Jones TV (2008) PIV Maps of Tip Leakage and Secondary Flow Fields on a Low-Speed Turbine Blade Cascade With Moving End Wall. J Turbomach 130:011001

[12] Gerolymos GA, Vallet I (1999) Tip-Clearance and Secondary Flows in a Transonic Compressor Rotor. J Turbomach. 121:751-762

[13] Gourdain N, Leboeuf F (2009) Unsteady Simulation of an Axial Compressor Stage with Casing and Blade Passive Treatments. J Turbomach 131:021013

[14] Jang CM, Furukawa M, Inoue M (2001a) Analysis of Vortical Flow Field in a Propeller Fan by LDV measurements and LES–Part I: Three-Dimensional Vortical Flow Structures. J Fluids Engineering, 123(4):748-754

[15] Jang CM, Furukawa M, Inoue M (2001b) Analysis of Vortical Flow Field in a Propeller Fan by LDV

measurements and LES–Part II: Unsteady nature of Vortical Flow Structures Due to Tip Vortex Breakdown. J Fluids Engineering 123(4):755-761
[16] You D, Wang M, Moin P, Mittal R (2006) Effects of Tip-Gap Size on the Tip-Leakage Flow in a Turbomachinery Cascade. Physics of Fluids 18: 105102
[17] You D, Wang M, Moin P, Mittal R (2007) Vortex Dynamics and Low-Pressure Fluctuations in the Tip-Clearance Fllow. J Turbomach. 129:1002-1014
[18] Miorini RL, Wu H, Katz J (2010) The Internal Structure of the Tip Leakage Vortex Within the Rotor of An Axial Waterjet Pump, draft submitted to the Turbo Expo 2010 conference, June 14-18, 2010, Glasgow, UK
[19] Wu H, Miorini RL, Katz J (2010) Measurements of the Tip Leakage Vortex Structures and Turbulence in the Meridional Plane of an Axial Water-Jet Pump, draft submitted to Experiments in Fluids
[20] Pope SB 2000 Turbulent Flows, Cambridge Press
[21] Meneveau C, and Katz J (2000) Scale-invariance and turbulence models for large-eddy simulation, Annu. Rev. Fluid Mech 32:1-32
[22] Smagorinsky, J. 1963, General Circulation Experiments with the Primitive Equations. Mon. Weather Rev. 91:99-164
[23] Chow YC, Uzol O, Katz J and Meneveau C (2005) Decomposition of the spatially filtered and ensemble averaged kinetic energy, the associated fluxes and scaling trends in a rotor wake. Physics of Fluids 17, 085102
[24] Uzol, O, Chow YC, Katz J. and Meneveau C, 2002, Unobstructed Particle Image Velocimetry Measurements within an Axial Turbo-Pump Using Liquid and Blades with Matched Refractive Indices. Experiments in Fluids Vol. 33, pp. 909-919
[25] Wu H, Soranna F, Michael T, Katz J and Jessup S, 2008, Cavitation Visualizes the Flow Structure in the Tip Region of a Waterjet Pump Rotor Blade, 27th Symposium on Naval Hydrodynamics, October 5-10, Seoul, Korea
[26] Roth G, Katz J (2001) Five Techniques for Increasing the Speed and Accuracy of PIV Interrogation. Meas. Sci. Technol. 12:238-245